AIP Journal of Applied Physics

Tomography of atomic number and density of materials using dual-energy imaging and the Alvarez and Macovski attenuation model

M. Paziresh, A. M. Kingston, S. J. Latham, W. K. Fullagar, and G. M. Myers

Citation: Journal of Applied Physics **119**, 214901 (2016); doi: 10.1063/1.4950807
View online: http://dx.doi.org/10.1063/1.4950807
View Table of Contents: http://scitation.aip.org/content/aip/journal/jap/119/21?ver=pdfcov
Published by the AIP Publishing

Tomography of atomic number and density of materials using dual-energy imaging and the Alvarez and Macovski attenuation model

M. Paziresh, A. M. Kingston,[a] S. J. Latham, W. K. Fullagar, and G. M. Myers
Department of Applied Mathematics, Research School of physics and Engineering, The Australian National University, Canberra 2601, Australia

(Received 11 February 2016; accepted 5 May 2016; published online 1 June 2016)

Dual-energy computed tomography and the Alvarez and Macovski [Phys. Med. Biol. **21**, 733 (1976)] transmitted intensity (AMTI) model were used in this study to estimate the maps of density (ρ) and atomic number (Z) of mineralogical samples. In this method, the attenuation coefficients are represented [Alvarez and Macovski, Phys. Med. Biol. **21**, 733 (1976)] in the form of the two most important interactions of X-rays with atoms that is, photoelectric absorption (PE) and Compton scattering (CS). This enables material discrimination as PE and CS are, respectively, dependent on the atomic number (Z) and density (ρ) of materials [Alvarez and Macovski, Phys. Med. Biol. **21**, 733 (1976)]. Dual-energy imaging is able to identify sample materials even if the materials have similar attenuation coefficients at single-energy spectrum. We use the full model rather than applying one of several applied simplified forms [Alvarez and Macovski, Phys. Med. Biol. **21**, 733 (1976); Siddiqui *et al.*, *SPE Annual Technical Conference and Exhibition* (Society of Petroleum Engineers, 2004); Derzhi, U.S. patent application 13/527,660 (2012); Heismann *et al.*, J. Appl. Phys. **94**, 2073–2079 (2003); Park and Kim, J. Korean Phys. Soc. **59**, 2709 (2011); Abudurexiti *et al.*, Radiol. Phys. Technol. **3**, 127–135 (2010); and Kaewkhao *et al.*, J. Quant. Spectrosc. Radiat. Transfer **109**, 1260–1265 (2008)]. This paper describes the tomographic reconstruction of ρ and Z maps of mineralogical samples using the AMTI model. The full model requires precise knowledge of the X-ray energy spectra and calibration of PE and CS constants and exponents of atomic number and energy that were estimated based on fits to simulations and calibration measurements. The estimated ρ and Z images of the samples used in this paper yield average relative errors of 2.62% and 1.19% and maximum relative errors of 2.64% and 7.85%, respectively. Furthermore, we demonstrate that the method accounts for the beam hardening effect in density (ρ) and atomic number (Z) reconstructions to a significant extent. *Published by AIP Publishing.* [http://dx.doi.org/10.1063/1.4950807]

I. INTRODUCTION

Imaging with two X-ray energy spectra, henceforth referred to as dual-energy imaging, is being adopted for material discrimination[2,3] and provides more information than conventional computed tomography (CT). Dual-energy material discrimination has found applications in the fields of medical imaging,[8] luggage screening,[9] and the petrochemical/mineral reservoir industry.[2]

Single-energy micro-CT (μ-CT) can provide micron resolution spatial structure images with a high signal-to-noise ratio (SNR) for determining the structure of samples but does not provide compositional information. In contrast, dual-energy imaging can provide three-dimensional (3D) maps of density and atomic number of constituent materials in a sample. Although single-energy CT may be used to discriminate between materials that have very different attenuation coefficients, some samples such as rocks can contain materials that have similar attenuation coefficients while their physical or transport properties are different. Atomic number and density mapping of a rock sample provide valuable input towards identifying the minerals present and their 3D distribution. This mineralogical and structural information is, in turn, essential to geological classification of sedimentary rock texture and subsequent alterations by diagenics processes during burial. The information is also essential for predicting the mechanical and flow properties of the rock and its pores using digital images. One of the main applications is the extraction of oil and gas from reservoir rocks, since the minerals and their distribution strongly affect properties such as wettability, which is highly relevant to recovery from conventional reservoirs by waterflooding, or brittleness, which dictates whether an unconventional reservoir is amenable to hydraulic fracturing. Single-energy imaging has limited ability to distinguish minerals such as quartz from feldspars or calcite from dolomite, which leads to uncertainties in modeling of geomechanical and transport properties.[10] If the attenuation coefficients vary differently with energy, dual-energy imaging can aid material discrimination.

Conventional reconstruction algorithms assume monochromatic radiation, but the X-ray radiation is often polychromatic and therefore the reconstructions will include visible evidences in the form of cupping artifacts (in cylindrical sample images) or streaking artifacts (between high density materials). The attenuation coefficient model used for dual-energy analysis is a function of energy and inherently accounts for beam hardening. This is evident in the resultant reconstruction of density and atomic number.

[a]Author to whom correspondence should be addressed. Electronic mail: andrew.kingston@anu.edu.au

There are two main mechanisms by which X-rays interact with matter in a typical μ-CT X-ray energy range of 10 to 120 keV. The photoelectric absorption (PE) dominates at lower energies (e.g., less than 30 keV for biological materials but increases with atomic number), while Compton scattering (CS) is more prevalent at higher energies. Alvarez and Macovski[1] modeled the attenuation coefficient (AMAC) of a material as a two-basis function that characterizes PE and CS. The material discrimination capability of dual-energy CT relies on the fact that PE depends strongly on atomic number (Z) and CS is proportional to density (ρ). The AMAC model has been used in various simplified forms.[1–7] Alvarez and Macovski[1] presented the full model but used a polynomial approximation of attenuation functions of projections of ρ and Z. Siddiqui and Khamees[2] simplified the model by assuming the data are collected at two monochromatic energies. Derzhi[3] applied a post-correction technique on Siddiqui's method using reference materials. Derzhi determined a functional relation between the atomic number and the density estimation by Siddiqui and Khamees method[2] and their relative error to estimate the optimal coefficients for the system of reference materials. They applied the corrections to reduce the error between estimated and real atomic number and density images of target materials. Heismann *et al.*[4] quantitatively estimated density as a weighted difference of attenuation coefficients at two distinct spectra, and atomic number as a non-linear function of the ratio of dual-energy attenuation coefficients.

In this paper, we investigate the model in its full unsimplified form, for material discrimination in rock samples. Section II covers the theoretical background of dual-energy imaging, adapting the attenuation coefficient model for dual-energy imaging and showing how it can provide material discrimination. The AMAC model needs *a priori* spectral information. Section III describes the simulation of X-ray dual-energy spectra and attenuation by materials between an X-ray source and a detector. Section IV calibrates the AMAC model using the simulation and establishes a benchmark for the model in terms of accuracy. Section IV A describes the parameter estimation for a given setup, applying the attenuation coefficient data of a set of reference materials obtained from the National Institute of Standards and Technology (NIST). Section IV B demonstrates the intensity model calibration using the simulated projections of cylinders, applying the same attenuation coefficients of the reference materials as in Section IV A. For the experimental protocol, Section IV C applies the collective calibration and spectral information to model the measured intensity. The relative error between this intensity model and the sample images captured at the Australian National University (ANU) μ-CT facility[11] is minimized to estimate the density and atomic number of each of the sample constituent materials, and Section V covers the estimation, segmentation, and analysis of ρ and Z maps of three rock samples: two sandstone and a carbonate.

II. ATTENUATION COEFFICIENT MODEL

The Beer-Lambert law describes the attenuation of monochromatic radiation as the line integral of attenuation coefficient (μ), as follows:[12]

$$\int_L \mu(\boldsymbol{s})d\boldsymbol{s} = -\ln\left(\frac{I}{I_0}\right), \tag{1}$$

where I_0 and I are the intensity of the incident and the transmitted radiation, respectively, along the X-ray propagation (L) as the beam travels through the thickness of sample materials ($\boldsymbol{s}$).

However, the attenuation coefficient (μ) is a function of energy (E), and X-ray radiation in a lab-based μ-CT system spans a range of wavelengths. Consequently, the Beer-Lambert law is adapted to account for the polychromatic nature of X-rays such that the transmitted intensity (I) is presented as follows:

$$I = -\int_0^{E_\varepsilon^{\max}} S_\varepsilon(E)\ \exp\left[-\int_L \mu(\boldsymbol{s},E)\mathrm{d}\boldsymbol{s}\right]\mathrm{d}E, \tag{2}$$

where $S_\varepsilon(E)$ of the energy label (ε) with X-ray of maximum energy ($E_\varepsilon^{\max}$) is the respective incident X-ray intensity spectrum modulated by detector quantum efficiency and spectral transmission of non-sample absorbing materials between source and detector (III).

In the X-ray radiation energy range [10, 120] keV, the three most important interactions of X-ray photons with matter are the photoelectric absorption, Compton scattering, and Rayleigh scattering. Photoelectric absorption occurs when an incident X-ray interacts with an electron of an atom of the material. The electron is ejected from that atom and the photon is totally absorbed.[13] Compton scattering occurs when the incident photon interacts with an electron. The electron is given part of the energy of the photon to recoil and the X-ray photon is scattered through a different angle with a different energy related to the angle, to conserve the mass-energy and momentum of the system.[13] Rayleigh scattering is the elastic scattering in which the photon energy is conserved and results in occasional redirection of the X-ray photon. Rayleigh scattering is more evident at lower energies because its scattering angle is larger at lower energies.[13] Relative to photoelectric absorption and Compton scattering, the Rayleigh scattering has negligible effect on the attenuation coefficient. Other X-ray absorption processes occur at higher energies that are generally not relevant in X-ray CT.

Alvarez and Macovski[1] modeled the attenuation coefficient, $\mu(E)$, as an energy-dependent linear combination of photoelectric absorption $[p(\boldsymbol{s},E)]$ and Compton scattering $[c(\boldsymbol{s},E)]$. Equation (3) specifies the energy dependency of $p(\boldsymbol{s},E)$ and $c(\boldsymbol{s},E)$ and their contribution to the total linear attenuation coefficients $\mu(\boldsymbol{s},E)$. In Equation (3), classically $m=3$ while for numerical fits to experimental data, m lies between 3 and 3.5.[14]

$$\mu(\boldsymbol{s},E) = \frac{p(\boldsymbol{s},E)}{E^m} + c(\boldsymbol{s},E)f_{\mathrm{KN}}(E), \tag{3}$$

where f_{KN} is the Klein-Nishina function,[15] i.e.

$$f_{\mathrm{KN}}(E) = \frac{1+\alpha}{\alpha^2}\left[\frac{2(1+\alpha)}{1+2\alpha}\right] + \frac{1}{2\alpha}\ln(a+2\alpha) - \frac{1+3\alpha}{(1+2\alpha)^2}; \quad \alpha = \frac{E}{510.975}\ \mathrm{keV}. \tag{4}$$

Henceforth, the Alvarez and Macovski attenuation coefficient model in Equation (3) is referred to as the AMAC model.

The photoelectric effect, $p(\boldsymbol{s},E)$, increases approximately with the cube of atomic number ($Z^{n-1}; n-1 \approx 3$) and Compton scattering, $c(\boldsymbol{s},E)$, is proportional to density (ρ). The exponent $(n-1)$ can be in the interval[3,4] for numerical fits to experimental data.[14] Equation (5) shows how the photoelectric and Compton absorbances vary with the ρ and Z of the sample material.

$$p(\boldsymbol{s},E) = K_1 \frac{Z}{A}\,\boldsymbol{\rho}\,\mathbf{Z}^{n-1}; \quad c(\boldsymbol{s},E) = K_2 \frac{Z}{A}\,\boldsymbol{\rho}. \tag{5}$$

Here, K_1 and K_2 are constants, A is the atomic weight of material, $\mathbf{Z} = Z(\boldsymbol{s})$, and $\boldsymbol{\rho} = \rho(\boldsymbol{s})$.

For compound sample materials, the effective atomic number (Z_{eff}) can be derived from AMAC model as follows:

$$Z_{\text{eff}} = \sqrt[n]{\sum_j f_j \mathbf{Z}_j{}^n}, \tag{6}$$

where f_j is the fraction of the electrons associated with each element j, that is, the fraction of number of atoms of element j multiplied by its atomic number over the total number of electrons of the molecule. The molecular weight (A_{eff}) is taken from NIST where $\left(\frac{Z_{\text{eff}}}{A\text{eff}} \simeq 0.5\right)$ in Equation 5. $\mathbf{Z}_j$ is the atomic number and $\mathbf{A}_j$ is the atomic weight of each element.

By substituting the AMAC model into Equation (2), we can estimate $\int_L p(\boldsymbol{s},E)$ and $\int_L c(\boldsymbol{s},E)$ and so reconstruct and segment the $\mathbf{Z}$ and $\boldsymbol{\rho}$ maps of constituent sample materials. This requires capturing the transmitted intensity image (I_ε) at photoelectric absorption and Compton scattering dominant energies with energy labels $\varepsilon \in \{\varepsilon_1, \varepsilon_2\}$. The mentioned intensity measurements, henceforth in this paper called Alvarez and Macovski transmitted intensity (AMTI) model, are according to the following equation:

$$I_\varepsilon = \int_{E=0}^{\varepsilon} S_\varepsilon(E) \exp\left[\frac{\int_L p(\boldsymbol{s},E)\,\mathrm{d}\boldsymbol{s}}{E^m} + \int_L c(\boldsymbol{s},E)\,\mathrm{d}\boldsymbol{s} f_{\text{KN}}(E)\right] \mathrm{d}E. \tag{7}$$

III. X-RAY ENERGY SPECTRUM MODEL

Solving the AMTI model (7) requires a model for $S_\varepsilon(E)$. It was simulated as follows: Bremsstrahlung was simulated using Kramer's law[16] and characteristic emission lines were added to approximate the spectrum from the tungsten target. This spectrum was then modulated by the spectral transmission of each non-sample absorbing material between the source and the detector. The X-ray tube was an "X-tek system limited RTR 225 keV" with 2 μm tungsten target material and 0.5 mm beryllium window. The detector was a Perkin Elmer "XRD 1621 scintillator-based area detector"[17] with 2048 $\times$ 2048 width $\times$ height pixels with square pixel width 0.2 mm. The camera to detector distance (CL) was 1000 mm for our imaging geometry. Consequently, the absorbing materials between source and detector were: 2 μm tungsten, 500 μm beryllium window on the X-ray source, 1000 mm air, and sensor protection materials (0.75 mm of aluminum and 0.75 mm of carbon fiber). Absorption due to the materials was modeled as[18] $\prod_i e^{-\mu_i(E)\,s_i}$, where $\mu_i(E)$ is the energy dependent absorption coefficient of absorbing materials taken from NIST and s_i is the thickness of the ith material. X-rays were further modulated by the attenuation of the detector's 650 μm cesium iodide scintillator $(1 - e^{-\mu_{sci}(E)\boldsymbol{s}_{sci}})$. An energy proportional detector (Flat Panel Perkin Elmer XRD 1621) was used, so the energy absorbed by the detector was modeled as

$$S_\varepsilon(E) = E \times \left[\frac{K}{2\pi c}\left(\frac{E_\varepsilon^{\max}}{E} - 1\right) + \sum_i k_j \delta(E - E_i)\right] \times \prod_i e^{-\mu_i(E)\,s_i} \times \left(1 - e^{-\mu_{sci}(E)\,\boldsymbol{s}_{sci}}\right). \tag{8}$$

The relative magnitude of Kramer's constant, K, and the emission line intensities, k_j, were adjusted based on attenuation corrected observation of source spectra, using a cadmium telluride (CdTe) detector (XR-100T-CdTe Amptek spectrum analyzer) after applying a stripping algorithm.[19]

Two energy spectra were simulated approximately as follows: (1) spectrum ε_1 with maximum energy of 60 keV and 0.5 mm Al filtering for which the photoelectric absorption effect is dominant, and (2) spectrum ε_2 with maximum energy of 120 keV and 0.35 mm Cu filtering, for which the Compton scattering dominates for $Z \lesssim 13$ as shown in Fig. 1. In an ideal case, the spectra should be chosen such that they distinctly correspond to photoelectric and Compton attenuation basis within the AMAC model. However, the polychromatic nature of the illuminated X-ray is less than ideal because the two spectra overlap in energy range between 30 and 60 keV.

IV. SIMULATION: VALIDATING AND CALIBRATING THE MODEL

We calibrated the AMAC model for our experimental setup using several readily available materials that span the

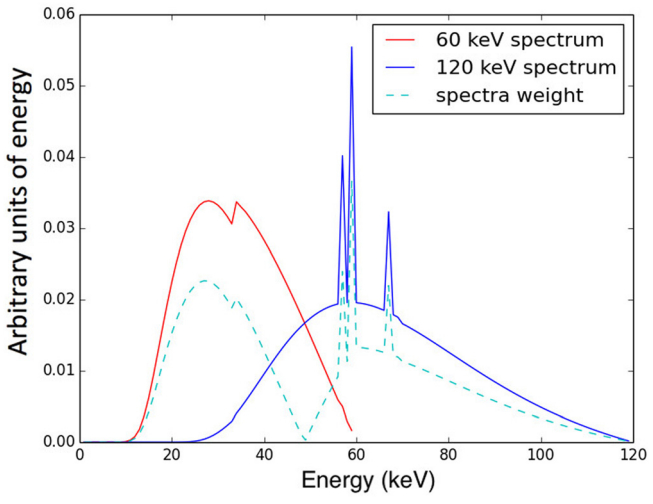

FIG. 1. Simulated dual-energy spectra at 60 (red line) and 120 keV (blue line) maximum energies modified to match that seen for our experimental protocol, and the spectra weight (dashed cyan line) which is added to the AMAC model in Section IV A.

Z and ρ ranges of interest for rocks. These are carbon (C), acrylic ($C_5O_2H_8$), teflon (C_2F_4), glass (SiO_2), aluminum (Al), marble ($CaCO_3$), and titanium (Ti). We analyse radiographs of cylindrical samples of these materials to find optimal values for K_1, K_2, m, and n. The estimation of m and n is partly motivated by the experimental setup. The choice of reference materials and the spectral weight function affect the estimation of m and n. First, in Section IV A, we have calibrated the AMAC model using our simulated spectra and attenuation coefficient data [$\frac{\mu(E)}{\rho}$] from NIST. This gives an estimate of parameter values, demonstrates the adequacy of the AMAC model (3), and establishes a benchmark on the attainable accuracy of ρ and Z_{eff}. In Section IV B, we then simulate the experiments to be used for calibration of the AMTI model (7) to show that our proposed method both (a) gives similar parameter values and (b) can attain the comparable accuracy. Finally, in Section IV C, we calibrate the AMTI model using the measured radiographs to demonstrate that our simulated spectra are accurate since again the parameter values and accuracy are comparable.

A. AMAC model calibration using NIST data

We are required to estimate the photoelectric absorption coefficient, K_1, Compton scattering coefficient, K_2, energy exponent constant, m, and atomic number exponent constant, n, for the AMAC model (3) using the selected reference materials and the two simulated spectra. K_1 and K_2 constants estimate the contribution of PE and CS effects to the model. The numerical fits to NIST data for m and n, subsequently, lie in the range [3, 3.5] and [3, 4].[14]

The attenuation coefficients (μ) of the reference materials (ω) were obtained from the NIST database in the energy range [1, 120] keV for the simulations. We fit (in a least square sense) the AMAC model (3) with the NIST data to calibrate the model for our reference materials as shown in Equation (9).

$$\underset{\{K_1,K_2,m,n\}}{\text{minimize}} \sum_{\varepsilon,\omega} W_\varepsilon(E) \parallel \mu^{\omega}_{\text{NIST}}(\boldsymbol{s},E) - \frac{p^{\omega}(\boldsymbol{s},E)}{E^m} - c^{\omega}(\boldsymbol{s},E) f_{\text{KN}}(E) \parallel^2. \tag{9}$$

Initially, titanium dominated the fits; therefore, to prevent excessive influence of materials with higher atomic number, the error calculation was modified to minimize the relative error i.e., $min\left(\frac{\delta_\mu}{\mu}\right)^2$. The estimated parameters are $K_1 = 13.96\left(\frac{\text{keV}^3\text{cm}^2}{\text{gr}}\right)$, $K_2 = 0.30\left(\frac{\text{cm}^2}{\text{gr}}\right)$, $m = 3.00$, and $n = 3.20$. Figure 2 shows a plot of attenuation coefficients according to NIST data (red line) and the model (dashed blue line) fits, applying the estimated K_1, K_2, m, and n constants for glass, acrylic, titanium, and marble to be discussed in this section.

To apply the spectra influence, we weighted Equation (9) with the absolute difference of the spectra [W(E)] as shown in Fig. 1 (dashed cyan line). This gives lower weight to the overlapping energy region between lower and higher energy spectra than the effective PE and CS regions (Fig. 1). Adding the spectra weight also means the maximum K-edge in our reference materials (Ti; approximately 5 keV) is avoided through applying spectra weight. For these simulations shown in Fig. 1 that model our experimental setup, the spectra start at about 10 keV so the K-edges do not impact the results when we apply the spectra weight to AMAC model calibration.

We note here that the AMAC model (3) does not account for increased absorption above the K-edges of materials. Within our range of reference materials, Ti has the highest K-edge at 4.99 keV and marble the next highest K-edge at 2.48 keV (see Figs. 2(c) and 2(d)). Figure 2(b) shows a plot of the fitting results for glass, which was one of the reference materials. Glass and aluminum have K-edges at 1.84 and 1.56 keV, respectively, which are well below the transmission energies in our setup. The average relative error between the AMAC model estimated attenuation coefficients and the NIST attenuation coefficients in the energy range [1, 120] keV is 16.50%; however, the relative error in energy range [10, 120] keV is 1.96% as shown in Table I. As noted, the inaccuracy is mostly because the model does not account for K-edge absorption of titanium and marble; therefore, our selected spectra (Fig. 1) reduced calibration error, due to K-edges, by approximately 14%.

We also note that using the attenuation coefficient values of AMAC model for calibration will result in totally compatible μ values with that of the model; however, using NIST attenuation coefficients for calibration (even after avoiding K-edges; energy range of [10, 120] keV) shows 1.96% average relative error between NIST and the model attenuation coefficients. In this case, the inaccuracy is mostly due to inadequacy of the AMAC model. The estimated atomic number is a mathematical model to best reflect the observed attenuation measurements, rather than an actual physical reality (e.g., there is no fractional atomic number elements).

B. AMTI model calibration using simulated cylinder images

We simulated radiographs ($P^{\omega}_{\varepsilon\{sim\}}$) of aluminum, carbon, marble, acrylic, carbon, glass, and titanium with 10.00, 6.08, 10.00, 9.90, 19.56, 10.00, 6.09 mm diameter cylinders of each reference material (with cylinder sizes and materials matching the physical experiments of Section V). The source to sample distances (SD) are 33.8, 17.3, 33.8, 34.5, 71, 35.2, 17.8 mm subsequently and camera length (CL) is 1000 mm for all cases. The attenuation coefficient values of materials are taken from the NIST attenuation coefficient curves. The samples were imaged using the cone beam X-ray radiation in a circle trajectory (shown in Fig. 3) at two different energies: 60 keV with 0.5 mm Al filter (S_{ε_1}) and 120 keV with 0.35 mm Cu filter (S_{ε_2}) (Fig. 1) with 1440 angles of projections.

We simulated ρ and Z_{eff} (6) projections of reference materials to build $\int_L p(\boldsymbol{s},E)\,\mathrm{d}s$ and $\int_L c(\boldsymbol{s},E)\,\mathrm{d}s$ projections (5). The atomic number and energy exponent values (m and n) are taken from Section IV A and applied to the AMTI model (10) to estimate K_1 and K_2 and validate the estimation of calibration parameters in Section IV A. K_1 and K_2 were obtained with a least-square fit using the relative error as follows:

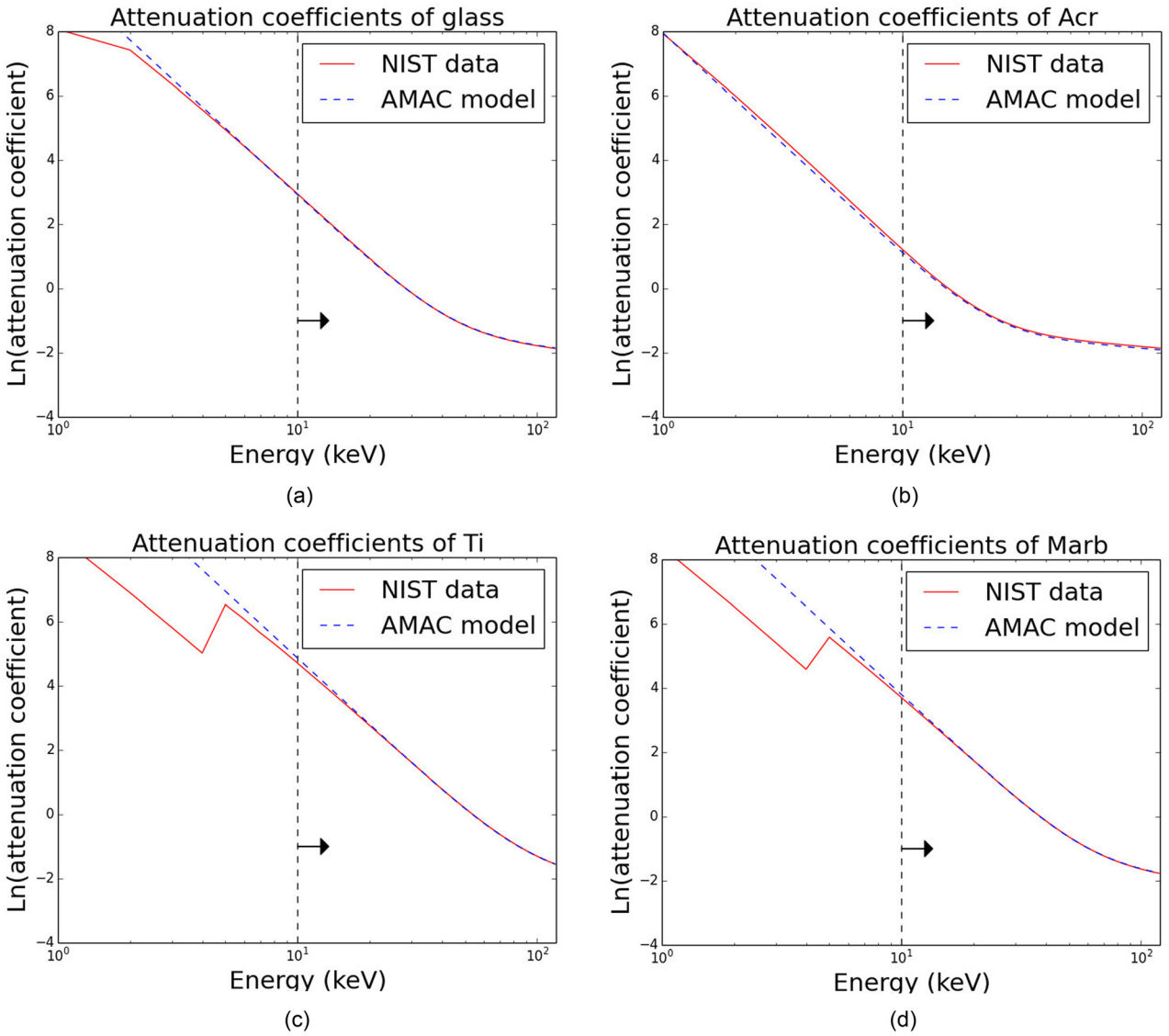

FIG. 2. Plot of $\ln(\mu)$ versus ($E = [1, 120]$ keV) of NIST data (red line) and AMAC model (blue dashed line) fits applying the estimated K_1, K_2, m, and n constants in Section IV A for (a) glass, (b) acrylic, (c) titanium, and (d) marble.

$$\underset{\{K_1,K_2\}}{\text{minimize}} \sum_{\varepsilon,\omega} \| P^{\omega}_{\varepsilon\{sim\}} - \int_{E=0}^{\varepsilon} S_{\varepsilon}(E) \exp\left[\frac{\int_L p^{\omega}(\boldsymbol{s},E)\,\mathrm{d}s}{E^m} + \int_L c^{\omega}(\boldsymbol{s},E)\,\mathrm{d}s f_{\mathrm{KN}}(E)\right] \mathrm{d}E \|^2. \quad (10)$$

PE and CS constants estimations are $K_1 = 13.94\left(\frac{\mathrm{keV}^3\,\mathrm{cm}^2}{\mathrm{gr}}\right)$ and $K_2 = 0.30\left(\frac{\mathrm{cm}^2}{\mathrm{gr}}\right)$ which shows AMTI model calibration is compatible with the AMAC model calibration using the simulated attenuation coefficient data from NIST and validates our proposed experimental calibration technique using cylinders of reference materials. Figure 4 shows a horizontal line through the simulated projection image of glass cylinder and the AMTI model fit on that. We have chosen to show the plots of material glass and marble because they are respectively close in atomic structure to

TABLE I. Relative error between NIST attenuation coefficient and AMAC model for reference materials.

Material names	Estimated model-data relative error in [1, 120] keV (%)	Estimated model-data relative error in [10, 120] keV (%)
Al	18.75	1.29
C	2.98	2.79
Marble	25.71	0.85
Acr	5.52	5.00
Teflon	1.81	1.23
Glass	5.80	1.26
Ti	54.98	1.29
Average	16.50	1.96

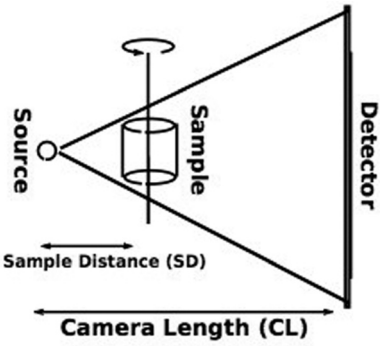

FIG. 3. The fine focus imaging geometry.

quartz in sandstones and calcite in carbonate rocks which will be examined in Section V.

To calculate density and atomic number of reference materials, the calibrated AMTI model (7) is matched with simulated projections of reference materials using Newton-Raphson optimization method[20] to estimate photoelectric $(\int_L p(\boldsymbol{s},E)\,\mathrm{d}s)$ and Compton $(\int_L c(\boldsymbol{s},E)\,\mathrm{d}s)$ projections of materials. The $\frac{Z}{A}\rho Z^{n-1}$ and $\frac{Z}{A}\rho$ images have been reconstructed by filtered back-projection and used to calculate the density and atomic number of each pixel of the image which may contain an element or a compound or a mixture of materials. In the case of compound or mixture materials, the effective atomic number can be derived using Equation (6).

We note here that there are several material dependent parameters (μ, Z_{eff}, and $\frac{Z}{A}\rho$) in the AMTI model which may affect both calibration and ρ and Z estimation using the model. Although the general structure of compound and mixture materials of our reference materials are known, we acknowledge some material composition uncertainty in our estimations. For instance, glass or borosilicate has the chemical structure of 80.60% silica (SiO_2), 12.60% boric oxide (B_2O_3), 4.20% sodium oxide (Na_2O), and 2.20% aluminum oxide (Al_2O_3), and 3.00% of (Fe_2O_3, CaO, MgO, Cl) according to the NIST database. We matched the chemical composition of our reference materials such that the $\mathrm{avg}\left(\frac{\delta_\rho}{\rho}\right)$ and $\mathrm{avg}\left(\frac{\delta_Z}{Z}\right)$ were as low as 0.61% and 0.77%; however, using the same calibration on experimental data resulted in increases of ρ and Z estimation average relative error to 4.28% and 2.75% for all reference materials. Therefore, we decided to retain the simulations close to experimental data. This way the average of material uncertainty error for all reference materials of experimental and simulated results is compatible.

Table II shows the average estimated density and their atomic numbers of the reference materials using simulated projections of cylinders of these materials data and their relevant theoretical ρ and Z values. The estimated results show errors as follows: $\mathrm{avg}\left(\frac{\delta_\rho}{\rho}\right) = 2.19\%$, $\mathrm{avg}\left(\frac{\delta_Z}{Z}\right) = 0.88\%$, $[\min,\max]\left(\frac{\delta_\rho}{\rho}\right) = [0.8\%, 5.73\%]$ and $[\min,\max]\left(\frac{\delta_Z}{Z}\right) = [0.28\%, 1.82\%]$. The calibrated AMAC model itself has about 1.96% average error for all materials in energy range of [10, 120] keV because of the inadequacy of the model. The average relative errors of estimated ρ and Z in this case are comparable. We have applied the estimated m and n values of this section for our experimental protocol in Secs. IV C and V. In Section IV C, we apply the calibrated model to experimental data of the same set of materials to estimate ρ and Z and compare the experimental results and simulated results. Then in Sec. V A, we analyze three types of rock cores using the method.

C. Testing the AMTI model calibration using the real cylinder images

We imaged the cylindrical samples of aluminum (Al), carbon (C), acrylic $(C_5O_2H_8)$, marble $(CaCO_3)$, teflon (C_2F_4), glass (SiO_2), and titanium (Ti) using the parameters of the experiment as described in Section IV B with the exposure time of 2 s and X-ray current of 100 mA for all cases.

In this section also, first we calibrate the intensity model (7) using experimental images to compare with the calibration

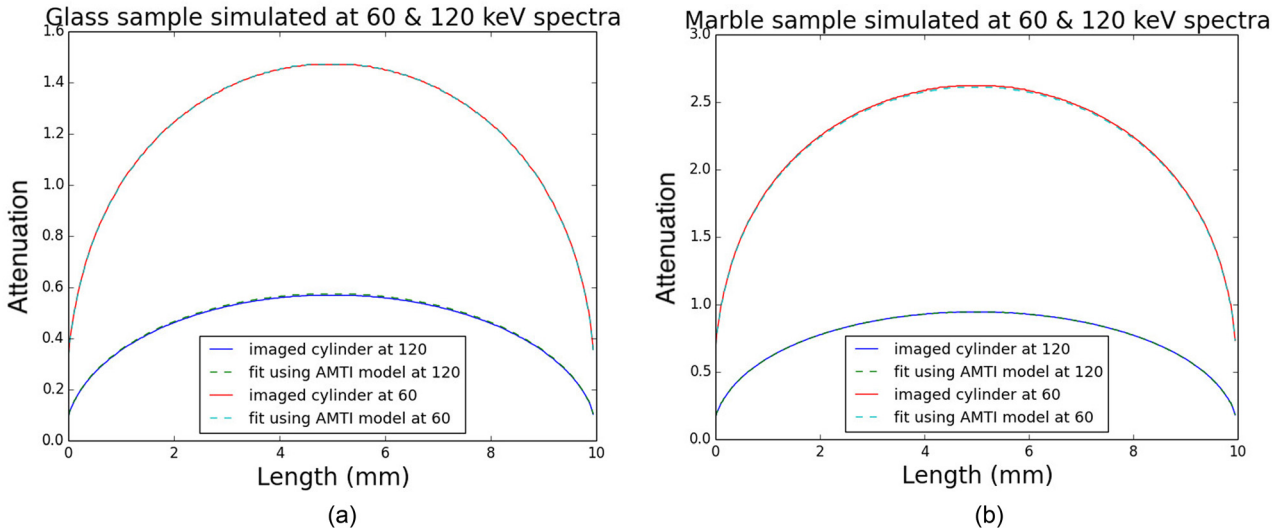

FIG. 4. A line through a simulated projection cylinder and the AMTI model fit: at 60 keV (red line and dashed cyan line) and 120 keV (blue and dashed green line) maximum energies for (a) glass and (b) marble.

TABLE II. Effective atomic number and bulk density of reference materials.

Material names	Estimated ρ using simulated data	Estimated ρ using real data	Theoretical ρ	Estimated Z using simulated data	Estimated Z using real data	Theoretical Z
Al	2.64	2.64	2.70	13.14	13.34	13.00
C	1.43	1.43	1.46	5.89	5.95	6.00
Marble	2.67	2.75	2.70	15.44	15.57	15.35
Acr	1.25	1.28	1.18	6.45	6.42	6.51
Teflon	2.13	2.08	2.15	8.43	8.50	8.45
Glass	2.19	2.20	2.23	11.77	11.48	11.65
Ti	4.58	4.58	4.50	21.90	21.90	22.00

of the simulated data in Sections IV A and IV B. The K_1 and K_2 values are estimated to be 13.50 $\left(\frac{\text{keV}^3\,\text{cm}^2}{\text{gr}}\right)$ and 0.29 $\left(\frac{\text{cm}^2}{\text{gr}}\right)$ subsequently which are comparable with the K_1 and K_2, the estimations in Sections IV A and IV B. This shows that the calibration of the AMAC model using NIST attenuation coefficients of reference materials (Section IV A), or calibration of the AMTI model using the simulated images of reference materials (Section IV B) has almost the same estimated values as in this section where we calibrated the AMTI model using the experimental images of reference materials. It also shows that we can calibrate the model for a set of reference materials and then compute the density and atomic number for one of the materials as shown in next paragraph, or even other materials as we will show in Section V A for rocks.

To estimate projections of $\rho\frac{Z^{n-1}}{A}$ and $\rho\frac{Z}{A}$, we have used the Newton-Raphson method to minimize the absolute error between the calibrated model (7) and experimental radiographs of the material samples. Using *a priori* information of materials, $\frac{Z}{A}$, we can obtain the ρ and Z projections. Figure 5 shows a horizontal line through the projection image of the glass sample and the model fit to that. This can be reconstructed using standard filtered back-projection to generate a two-channel (ρ, Z) volume image of the sample. Table II shows average ρ and Z estimation applying the real data in this section. It also shows average ρ and Z estimation of Section IV B using simulated cylinder images and the theoretical values for comparison. The density and the atomic number error intervals are [0.97%, 7.85%] and [0.45%, 2.64%], respectively, with an average relative error of 2.87% and 1.26%. The results using the real data are comparable with the results of simulations in Sections IV A and IV B. This means that the ρ and Z estimations of a sample constituent materials using the calibrated full model (7) can be used to identify the materials by comparing to a database of theoretical ρ and Z values of materials (future work).

V. EXPERIMENTAL ANALYSIS

In this section, we apply the same method as in Section IV C to calculate density and atomic number distributions in several rock samples including Bentheimer and Berea sandstones and a carbonate. We imaged the radiographs ($P^{\omega}_{\varepsilon\{sim\}}$) of material ($\omega$), that is Bentheimer sandstone, Berea sandstones, or the carbon cylinders, with 10 mm diameter. The source to sample distance (SD) are 35 mm for Bentheimer and Berea sandstones and 13 mm for the carbonate sample. Camera length (CL) is 1000 mm for all cases. The samples were imaged at two different energies: 60 keV with 0.5 mm Al filter (S_{ε_1} and 120 keV with 0.35 mm Cu filter S_{ε_2}) (Fig. 1). The X-ray current was the same at both 60 and 120 keV, but was varied depending on the material: Berea was imaged at 80 mA, while Bentheimer and the carbonate were imaged at 100 mA. The X-ray exposure time for Bentheimer, Berea,

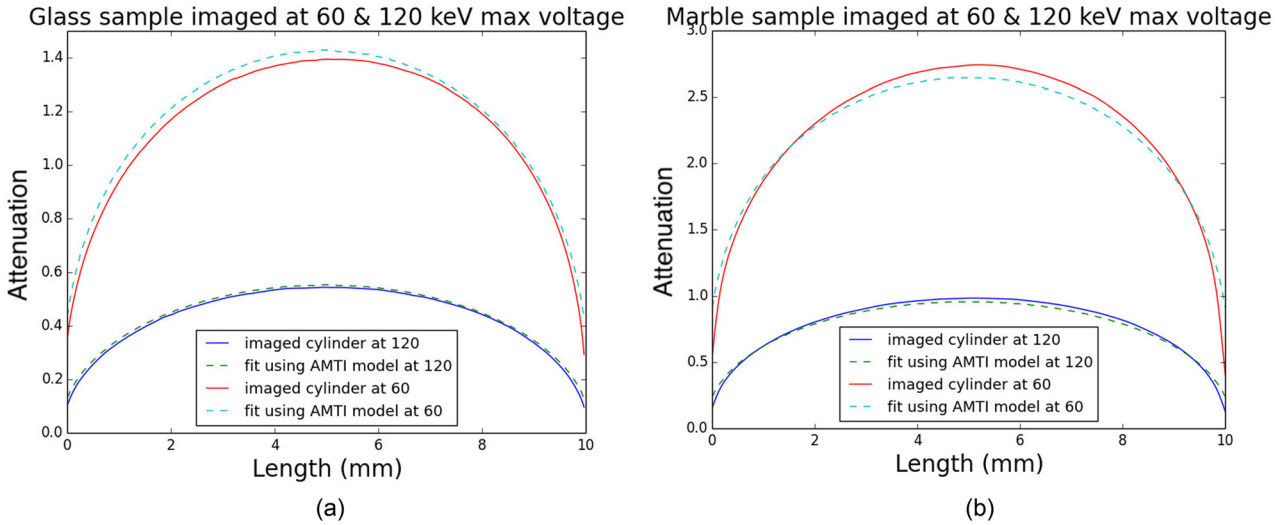

FIG. 5. A line through an imaged projection cylinder and the AMTI model fit: at 60 keV (red line and dashed cyan line) and 120 keV (blue and dashed green line) maximum energies for (a) glass and (b) marble.

and the carbonate samples, respectively, were 3.2, 4, and 3.2 s for 60 keV radiation and 2, 2.5, and 2 s for 120 keV radiation. The total number of projections was imaged within one circle trajectory (shown in Fig. 3) at 1440 angles for Bentheimer and Berea sandstones and at 2880 angles for the carbonate sample. We linearized the projection data and applied alignment,[21] auto-focus,[22] and drift correction.[23] The projection data also masked for the region outside the sample cylinder. Where the estimated atomic number and the density using AMTI model were less than or equal to zero, we regularized ρ and Z values with 1×10^{-3} and 12×10^{-5} (using 12 as the rounded up average atomic number of reference materials).

We used parameters K_1 and K_2 from Section IV C and m and n from Section IV A in the model (7). I_ε are radiographs of rock samples (I_{ε_1} and I_{ε_2}). The absolute error between the calibrated model and I_ε is minimized using Newton-Raphson method to estimate the projections of $\rho\frac{Z^{n-1}}{A}$ and $\rho\frac{Z}{A}$. The atomic number and the density 3D images of Bentheimer, Berea, and carbonate were reconstructed using Katsevich filtered back-projection reconstruction method.[24,25] We applied the single-phase (quartz) segmentation of ρ and Z tomograms in Bentheimer and Berea sandstones and dual-phase segmentation (calcite and dolomite) in the carbonate. We determined the average of each segment for ρ and Z as shown in Figs. 7(a-iii) and 7(b-iii).

A. Material discrimination of rock

The main component of sandstones is quartz so we apply a single-phase segmentation for Bentheimer and Berea sandstones. For each of the ρ and Z reconstructed images, a 2D histogram of neighborhood-mean versus neighborhood standard-deviation is calculated. The standard-deviation value where the 2D histogram forms peaks is used as an estimate of the image noise, $\hat{\sigma_\rho}$ and $\hat{\sigma_Z}$. The neighborhood standard-deviation images (one for ρ tomogram and one for Z tomogram) are thresholded ($<1.25 * \hat{\sigma_\rho}$ and $<1.25 * \hat{\sigma_Z}$, respectively). The pair of image masks are combined into a single image mask via logical-and operation. The ρ and Z images are masked, and a Gaussian distribution is fit to the truncated histogram (truncated around the relevant quartz ρ (or Z) value).

For the Bentheimer sandstone, the mean of the segmented quartz density and the atomic number map using the above mentioned method, shown in Table III, have relative error of 2.64% and 1.44%, respectively.

The segmented quartz in Berea sandstone shows the mean $\rho = 2.64$ with $\hat{\sigma_\rho} = 0.23$ and $Z = 11.79$ with $\hat{\sigma_\rho} = 0.48$ which include a relative error of 0.37% and 0.08%, respectively. A slice through reconstruction of ρ and Z image of Berea is shown in Figs. 6(a-ii) and 6(b-ii). The estimated relative errors show the estimated results using the full model (7) provide good indication of the segmented material.

TABLE III. Effective atomic number and bulk density of materials.

Material names	Estimated ρ	Theoretical ρ	Estimated Z	Theoretical Z
Bentheimer (quartz)	2.72	2.65	11.61	11.78
Berea (quartz)	2.64	2.65	11.79	11.78
Carbonate (calcite)	2.57	2.71	15.23	15.71
Carbonate (dolomite)	2.81	2.87	13.41	13.74

The sample material of rocks is unknown so we considered the constituent material $\frac{Z}{A}$ value to be 0.5 because the $\frac{Z}{A}$ of quartz is about 0.499. The Z values can still be estimated independent of $\frac{Z}{A}$ value.

The third sample rock is carbonate which consists of calcite and dolomite. For dual-phase segmentation of the carbonate, the masking process is the same but fitting the mixture model is more involved. First, a mixture model of two Gaussians is fit to the Z image (parameters are two weights, two means, one standard deviation). A two-Gaussian mixture is also fit to the masked ρ image histogram, but with only one parameter (the standard deviation). The weights from the Z mixture module fit are used for the ρ mixture model. The mean values for the ρ mixture model are calculated by further masking the ρ image. The first and second ρ mean is calculated, respectively, by masking +/− one standard deviation of the first and second Z-mean.

Calcite and dolomite have very similar attenuation coefficients which make it difficult to distinguish in a single-energy imaging (see the reconstruction of carbonate sample imaged at 120 keV in Fig. 7(a-i) compared to segmented image in Fig. 7(b-i)). The atomic number of calcite is estimated to be 13.41 with $\hat{\sigma_Z} = 0.55$ and dolomite is 15.23 with $\hat{\sigma_Z} = 0.55$ which shows relative error of 5.16% and 2.09%, respectively. The calcite and dolomite density estimation using the full AMTI model is 2.57 $(\mathrm{gr/cm^3})$ and dolomite density is 2.81 $(\mathrm{gr/cm^3})$ which contains 3.05% and 2.40% relative error, respectively. The calcite density relative error shows higher value than the maximum estimated relative error for reference materials. This is due to (1) the carbonate sample tilted between the two scans. This causes the rotation axis to pass through the rock at a different angle and makes accurate registration of projections impossible. The reconstruction is consequently poor at edges (as can be seen in Fig. 7(b-ii)). The segmentation/analysis method described above accounts for this as much as possible; (2) the fact that calcite is the predominant phase of the carbonate sample as shown in segmentation (Fig. 7(b-i)) and the segmented calcite may contain micro-scale air pores and clay which reduce the accuracy of our estimations; and (3) the heavy filtering of 0.35 mm Cu used for $\varepsilon_2 = 120$ keV spectra which reduce signal-to-noise (SNR) ratio. Since the dominant physical interaction of X-ray with matter in the range of ε_2 is Compton scattering which is dependent on ρ, the ρ image is consequently noisy. Calcite and dolomite have similar density values. In this case, atomic number estimations enable materials discrimination and even identification well, as shown in Fig. 7(a-ii); dolomite is clearly visible as dark patches in the slice through the estimated atomic number reconstruction, compatible with the segmented dolomite regions of Fig. 7(b-i).

The estimation of material properties via the full model is accurate with average relative error of 2.15% for the above mentioned rock samples which make material discrimination possible but the ρ images are noisy due to heavy filtering. This can be seen (along with the effect of the sample movement) in the results of the Carbonate presented in Fig. 7(b-ii).

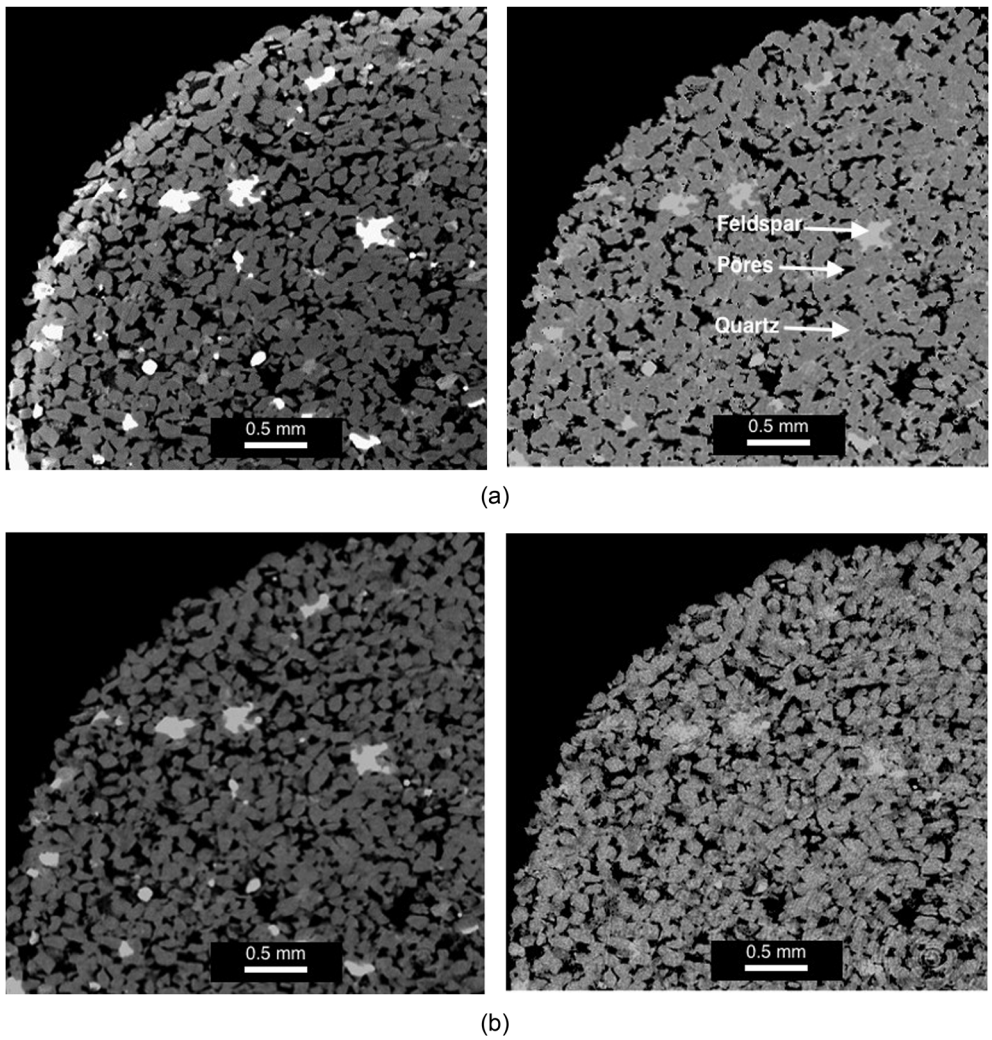

FIG. 6. (a-i) Reconstructed slice of Berea sandstone at $E_{\varepsilon}^{\max} = 60\,\text{keV}$, (b-i) reconstructed slice Berea sandstone at $E_{\varepsilon}^{\max} = 120\,\text{keV}$, (a-ii) reconstructed slice of the estimated Z using the AMTI model 7, and (b-ii) reconstructed slice of the estimated ρ using the AMTI model.

B. Beam hardening correction

Conventional reconstruction algorithms assume monochromatic radiation, while the X-ray is a function of energy as shown in spectra simulation of Fig. 1. This causes inconsistent values in the reconstructed images because physically the lower energy radiation is being attenuated as it passes through the material which leaves harder X-rays. This appears in the form of cupping and/or streaking artifacts in the reconstructed images. Figure 6(ii) shows cupping artifacts around the edges of the slice through the reconstructed image of Berea sandstone captured at 60 keV. An indication of the performance of the model can be seen in the lack of the beam-hardening artifacts in the reconstructions of ρ and Z volumes. The AMTI model (7) in its full form is a function of energy and should model beam hardening effect. The beam hardening correction is analytical over the broad spectra, and thus inherently superior to single-energy approximate correction methods. This is a direct benefit of the full model that inherently accounts for the beam-hardening in the projections of $\left(\frac{0.5}{\frac{Z}{A}}\right)\rho Z^{m-1}$ and $\left(\frac{0.5}{\frac{Z}{A}}\right)\rho\,\left(\left(\frac{0.5}{\frac{Z}{A}}\right) \simeq 1\right)$. The beam hardening artifact shown in Fig. 6(a-i) is corrected in the Z and ρ reconstructions in Figs. 6(a-ii) and 6(b-ii).

VI. CONCLUSION

The Alvarez and Macovski model has been used broadly for material discrimination purposes in a simplified form (e.g., 1–7). Here, we have applied the Alvarez and Macovski model in its full form. We calibrated the photoelectric absorption coefficient (K_1), Compton scattering coefficient (K_2), energy exponent (m), and atomic number exponent (n) by fitting the full AMAC model and the NIST attenuation coefficient data for a particular setup of reference materials. The relative error between the AMAC model and the NIST attenuation coefficient data shows 1.92% and 5.00% of average and maximum error. This shows an inherent error in the model.

The maximum error occurs for acrylic which does not fit the model well. The relative error in the estimated density of acrylic using the simulated cores in Section IV B and real imaged cylinders in Section IV C subsequently are 5.73% and 7.85% which exceeds the average relative error.

We also calibrated the AMTI model using the simulated projections of cylinders of the reference materials. We applied the calibrated AMTI model to estimate the ρ and Z projections of materials which are later reconstructed to ρ

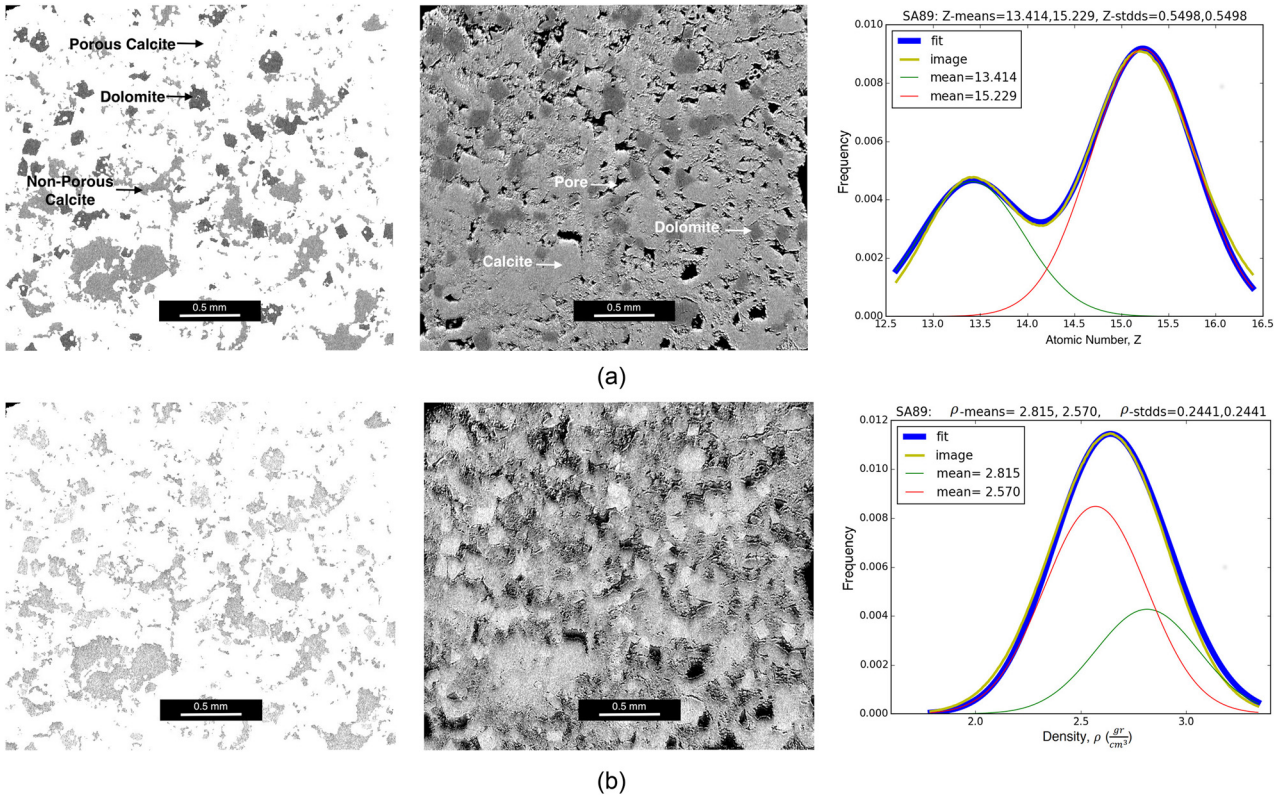

FIG. 7. (a-i) Reconstructed slice of the carbonate masked Z, (b-i) reconstructed slice of the carbonate masked ρ, (a-ii) reconstructed slice of the estimated Z using the AMTI model 7, (b-ii) reconstructed slice of the estimated ρ using the AMTI model, (a-iii) the plot of fitted Gaussian to histogram of masked Z, and (b-iii) the plot of fitted Gaussian to histogram of masked ρ.

and Z images. The accuracy benchmark shows the AMTI model has 1.96% and 5.00% average and maximum relative error for ρ estimation and 0.88% and 1.82% average and maximum relative error for Z estimation.

We also applied the calibrated the AMTI model to estimate ρ and Z projections of three rocks (Bentheimer and Berea sandstone and a carbonate). We reconstructed 3D projections using filtered back-projection. To obtain the ρ and Z maps of the main components of rocks (quartz in sandstones and calcite and dolomite in carbonate), we masked the ρ and Z tomograms to exclude "material-boundary" voxels determined by standard deviation of local grey levels and fitted Gaussians to the histograms of the masked images. The segmented ρ and Z regions include 2.80% and 1.50% relative average density and atomic number estimation error.

In this paper, we showed that given precise knowledge of spectra, the AMTI model is able to differentiate and identify materials via the ρ and Z mapping even if the constituent materials have similar attenuation coefficients in one energy spectra, provided their ρ and/or Z values vary. However, the proposed model calculations require precise knowledge of spectra and reference materials including $\frac{Z}{A}$ value for the unknown rock sample; it has some benefits such as: (1) The model reasonably corrected beam hardening effect in reconstructed ρ and Z images. (2) It can yield a good average estimated ρ and Z material properties with average of 2.62% and 1.19% with maximum of 7.85% and 2.64% of expected values, respectively, and (3) the materials are still identifiable through Z estimation even if the ρ of two constituent materials of sample having similar values and Z is not dependent on $\frac{Z}{A}$. Also, Z estimations are 1.43% more accurate in average than ρ estimations because the images captured at 120 keV suffer from low SNR due to the heavy filtering at high voltage. For further improvement, we plan to apply an iterative modification of the density and atomic number estimations on material matching with a material dictionary. In the reconstruction algorithm, we include an iterative update on the initial ρ and Z estimations of materials through the full model and a probabilistic classification to manage the materials distributions based on the material library.[26]

ACKNOWLEDGMENTS

The authors wish to thank Michael Turner and Andrew Fogden for their assistance and advice in sample preparation, μ-CT imaging, and petrophysics explanations. S.J.L., G.R.M., and A.M.K. acknowledge funding through the DigiCore consortium and the support of a linkage grant (LP150101040) from the Australian Research Council and FEI Company.

[1]R. E. Alvarez and A. Macovski, "Energy-selective reconstructions in x-ray computerised tomography," Phys. Med. Biol. **21**, 733 (1976).
[2]S. Siddiqui, A. A. Khamees *et al.*, "Dual-energy CT-scanning applications in rock characterization," in *SPE Annual Technical Conference and Exhibition* (Society of Petroleum Engineers, 2004).
[3]N. Derzhi, "Method for estimating effective atomic number and bulk density of rock samples using dual energy x-ray computed tomographic imaging," U.S. patent application 13/527,660 (2012).
[4]B. Heismann, J. Leppert, and K. Stierstorfer, "Density and atomic number measurements with spectral x-ray attenuation method," J. Appl. Phys. **94**, 2073–2079 (2003).

[5]J. S. Park and J. K. Kim, "Calculation of effective atomic number and normal density using a source weighting method in a dual energy x-ray inspection system," J. Korean Phys. Soc. **59**, 2709–2713 (2011).
[6]A. Abudurexiti, M. Kameda, E. Sato, P. Abderyim, T. Enomoto, M. Watanabe, K. Hitomi, E. Tanaka, H. Mori, T. Kawai *et al.*, "Demonstration of iodine k-edge imaging by use of an energy-discrimination x-ray computed tomography system with a cadmium telluride detector," Radiol. Phys. Technol. **3**, 127–135 (2010).
[7]J. Kaewkhao, J. Laopaiboon, and W. Chewpraditkul, "Determination of effective atomic numbers and effective electron densities for Cu/Zn alloy," J. Quant. Spectrosc. Radiat. Transfer **109**, 1260–1265 (2008).
[8]T. R. Johnson, B. Krauss, M. Sedlmair, M. Grasruck, H. Bruder, D. Morhard, C. Fink, S. Weckbach, M. Lenhard, B. Schmidt *et al.*, "Material differentiation by dual energy CT: Initial experience," Eur. Radiol. **17**, 1510–1517 (2007).
[9]Z. Ying, R. Naidu, K. Guilbert, D. Schafer, and C. R. Crawford, "Dual energy volumetric x-ray tomographic sensor for luggage screening," in *SAS'07 IEEE Sensors Applications Symposium, 2007*. (IEEE, 2007), pp. 1–6.
[10]A. N. Golab, M. A. Knackstedt, H. Averdunk, T. Senden, A. R. Butcher, and P. Jaime, "3D porosity and mineralogy characterization in tight gas sandstones," Leading Edge **29**, 1476–1483 (2010).
[11]A. Sakellariou, T. J. Senden, T. J. Sawkins, M. A. Knackstedt, M. L. Turner, A. C. Jones, M. Saadatfar, R. J. Roberts, A. Limaye, C. H. Arns *et al.*, "An x-ray tomography facility for quantitative prediction of mechanical and transport properties in geological, biological, and synthetic systems," Proc. SPIE **5535**, 473–484 (2004).
[12]A. Beer, "Determination of the absorption of red light in colored liquids," Ann. Phys. Chem. **162**, 78–88 (1852).
[13]F. H. Attix, *Introduction to Radiological Physics and Radiation Dosimetry* (John Wiley & Sons, 2008).
[14]Z. Cho, C. Tsai, and G. Wilson, "Study of contrast and modulation mechanisms in x-ray/photon transverse axial transmission tomography," Phys. Med. Biol. **20**, 879 (1975).
[15]O. Klein and Y. Nishina, "The scattering of light by free electrons according to Dirac's new relativistic dynamics," Nature **122**, 398–399 (1928).
[16]H. A. Kramers, "XCIII. On the theory of x-ray absorption and of the continuous x-ray spectrum," London, Edinburgh, Dublin Philos. Mag. J. Sci. **46**, 836–871 (1923).
[17]P. P. Brochure, "XRD 1621 N ES Series," Freemont, CA, USA (2012); available at http://www.perkinelmer.com/imaging-components/detectors/xrd-a-si/1621-xn.html.
[18]K. R. Spangenberg, *Vacuum Tubes* (McGraw-Hill, New York, 1948), Vol. 1.
[19]R. H. Redus, J. A. Pantazis, T. J. Pantazis, A. C. Huber, and B. J. Cross, "Characterization of CdTe detectors for quantitative x-ray spectroscopy," IEEE Trans. Nucl. Sci. **56**, 2524–2532 (2009).
[20]V. S. Ryaben'kii and S. V. Tsynkov, *A Theoretical Introduction to Numerical Analysis* (CRC Press, 2006).
[21]A. Kingston, A. Sakellariou, T. Varslot, G. Myers, and A. Sheppard, "Reliable automatic alignment of tomographic projection data by passive auto-focus," Med. Phys. **38**, 4934–4945 (2011).
[22]A. Kingston, A. Sakellariou, A. Sheppard, T. Varslot, and S. Latham, "An auto-focus method for generating sharp 3D tomographic images," Proc. SPIE **7804**, 78040J (2010).
[23]G. R. Myers, A. M. Kingston, T. K. Varslot, and A. P. Sheppard, "Extending reference scan drift correction to high-magnification high-cone-angle tomography," Opt. Lett. **36**, 4809–4811 (2011).
[24]A. Katsevich, "Analysis of an exact inversion algorithm for spiral cone-beam CT," Phys. Med. Biol. **47**, 2583 (2002).
[25]T. Varslot, A. Kingston, A. Sheppard, and A. Sakellariou, "Fast high-resolution micro-ct with exact reconstruction methods," Proc. SPIE **7804**, 780413 (2010).
[26]B. Recur, M. Paziresh, G. Myers, A. Kingston, S. Latham, and A. Sheppard, "Dual-energy iterative reconstruction for material characterisation," Proc. SPIE **9212**, 921213 (2014).